

# Undulation-induced moiré superlattices with 1D polarization domains and 1D flat bands in 2D bilayer semiconductors

Xingfu Li<sup>1</sup>, Sunny Gupta<sup>1</sup>, and Boris I. Yakobson<sup>1,2,3,\*</sup>

<sup>1</sup>*Department of Materials Science and Nanoengineering, Rice University, Houston, TX, 77005 USA*

<sup>2</sup>*Department of Chemistry, Rice University, Houston, TX 77005, USA*

<sup>3</sup>*Smalley-Curl Institute for Nanoscale Science and Technology, Rice University, Houston, TX, 77005 USA*

\*Email: biy@rice.edu

## ABSTRACT

Two-dimensional (2D) materials have a high Föppl–von Kármán number and can be easily bent, much like a paper, making undulations a novel way to design distinct electronic phases. Through first-principles calculations, we reveal the formation of 1D polarization domains and 1D flat electronic bands by 1D bending modulation to a 2D bilayer semiconductor. Using 1D sinusoidal undulation of a hexagonal boron nitride (*h*BN) bilayer as an example, we demonstrate how undulation induces nonuniform shear patterns, creating regions with unique local stacking and vertical polarization akin to sliding-induced ferroelectrics observed in twisted moiré systems. This sliding-induced polarization is also observed in double-wall BN nanotubes due to curvature differences between inner and outer tubes. Furthermore, undulation generates a shear-induced 1D moiré pattern that perturbs electronic states, confining them into 1D quantum-well-like bands with kinetic energy quenched in modulation direction while dispersive in other directions (1D flat bands). This electronic confinement is attributed to modulated shear deformation potential resulting from tangential polarization due to the moiré pattern. Thus, bending modulation and interlayer shear offer an alternative avenue, termed "curvytronics", to induce exotic phenomena in 2D bilayer materials.

## Introduction

Van der Waals structures,<sup>1</sup> consisting of two-dimensional (2D) materials stacks with precise control over monolayer elements, thickness, and interlayer alignment, offers a unique platform for discovering exotic physical effects not present in the individual counterparts. One such system, twisted bilayers with moiré patterns arising from a small mismatch in the layers' periodicity have led to several paradigm-shifting physical phenomena, referred as twistrionics.<sup>2</sup> The long-wavelength moiré period results in electronic flat bands, facilitating the study of strongly-correlated physics.<sup>3,4</sup> Additionally, twisting materials with intrinsic broken inversion symmetry, ranging from transition metal dichalcogenides to hexagonal boron nitride (*h*BN) and beyond,<sup>5</sup> creates domains with permanent and switchable electric polarization, an effect coined slidetronics,<sup>6</sup> with potential in ultrathin nonvolatile memory and computing devices. With twisted bilayer systems being extensively explored, we probe a distinct perturbation form, namely, bilayers that are periodically bent. Periodically bent bilayers are also expected to exhibit moiré patterns and artificial lattices due to changes in interlayer shear and local

stacking. However, unlike twists, which produces 2D moiré patterns, uniaxial periodic bending of bilayers with zero Gaussian curvature can generate 1D moiré patterns, leading to artificial electronic states, such as 1D quantum wells and 1D ferroelectric domains, unattainable through twisting.<sup>7</sup>

Bending 2D monolayers with non-zero Gaussian curvature has been an endeavor to create non-uniform strain pattern for generating pseudo-magnetic field,<sup>8-15</sup> altering electronic structure and triggering exotic phases,<sup>16-18</sup> such as Landau-level-like flat bands,<sup>9,10,13</sup> correlated electronic states,<sup>10,14</sup> valley Hall effect<sup>11,12</sup> and so on. Whether bending is achieved by suspending samples,<sup>19</sup> loading them onto substrates,<sup>20</sup> or using profiled substrates,<sup>11,15,21</sup> an intralayer strain field is induced by local changes of bond lengths in the resultant artificial flexural lattices, raising potential mechanical stability issues of retaining such intralayer strains. This raises the question of whether artificial electronic states and phases can appear from pure shear in the absence of a modification to bond length, i.e., without intralayer strain. The Föppl–von Kármán number, which indicates the ratio between in-plane stiffness and out-of-plane bending stiffness, for typical 2D materials is  $\gg 1$ ,<sup>22</sup> similar to a paper, signifying that 2D materials can easily bend without stretch or shrink. By bending bilayer with zero Gaussian curvature, a shear gradient is expected to form while ruling out interlayer strain, where the novel effects on electronic behavior have yet to be explored.

Here, by first-principles calculations, we explore the electronic properties of a periodically bent 2D bilayer with interlayer shear but no intralayer strain. Using an undulated *h*BN bilayer, a prototype 2D semiconductor as an example, we demonstrate that 1D undulation creates 1D moiré patterns due to variations in local stacking from the interlayer shear gradient. These undulations form regions with different vertical electric polarizations, resembling 1D ferroelectric domains. Similar polarization domains also appear in BN nanotubes (BNNT), where stacking changes along the circumference lead to alternating electric polarization. Besides 1D polarization domains, the 1D moiré pattern induces long-range potential and 1D electronic confinement, creating 1D bands – flat in the modulated direction but dispersive in the unmodulated one, exhibiting peculiar van Hove singularities in the density of states (DOS). These undulated 2D systems, akin to 1D quantum wells, are easier to create by mechanically bending bilayers, without intricate synthesis. This work opens new avenues to create novel electronic phases such as 1D ferroelectric domains and 1D quantum-well-like electronic states using undulated 2D bilayers, thereby going beyond what's achievable with twists. We refer to our approach as "curvytronics", in a similar spirit to twistronics and straintronics.

## Results and discussions

**Undulation-induced slidetronics** - A flat *h*BN bilayer can have *R*-type or *H*-type stacking based on the angle ( $\varphi$ ) between its layers ( $\varphi = 0^\circ$  for *R*-type, and  $\varphi = 60^\circ$  for *H*-type). *R*-type stacking (eclipsed configuration with B(N) over B(N)) breaks inversion symmetry, and upon sliding the layers, loses additional out-of-plane mirror symmetry, leading to the emergence of out-of-plane polarization (polarization refers to electric polarization). In contrast, *H*-type stacking maintains inversion symmetry

and does not exhibit any out-of-plane polarization, regardless of sliding. Fig. 1a shows a 2D map of the sliding potential step  $\Delta V_{sl}$  across an *R*-type flat *h*BN bilayer as one layer translates. The resulting distinct stacking configuration is indexed by a pair of sliding ratios,  $(v_{zz}, v_{ac})$ , defined as  $v_{zz} = x_{zz}/c_{zz}$  and  $v_{ac} = x_{ac}/c_{ac}$ , where  $x$  is the respective sliding distance and  $c$  is the lattice constant. *R*-type stacking in a rectangular unit cell is used as the reference  $(0, 0)$ . Specifically, AB  $(1/3, 0)$  and BA  $(2/3, 0)$  stacking (see Fig. 1b inset) exhibit the largest and opposite potential steps. This out-of-plane polarization can be toggled by sliding between stacking geometries, with implications for ferroelectric applications.<sup>23,24</sup> Similarly, undulating a 2D bilayer changes interlayer shear, leading to different local stackings, and thus a similar out-of-plane polarization is expected in undulated *R*-type *h*BN bilayers.

To explore the aforementioned effect, we consider *h*BN bilayer undulated into sinusoidal shapes  $f(x) = h\sin(2\pi x/L)$ , with different amplitudes  $h$  and periodic lengths  $L$ . The atomic structures are designed based on parallel curves with the interlayer distance fixed at 3.25 Å and bond length at 1.45 Å (more details of constructing geometries in SI-1). In resultant structures, as shown in Fig. 1c, atoms align along the parallel curved surfaces. In these structures, atoms on the left side of the supercell maintain the initial stacking, while interlayer shear increases and then decreases toward the right side, where atoms return to the initial stacking. The distinct shear patterns, characterized by the sliding ratio profiles throughout the undulated bilayer, for two bending degrees ( $h = 3$  Å and 6 Å with the same  $L$ ) are illustrated in Fig. 1d.

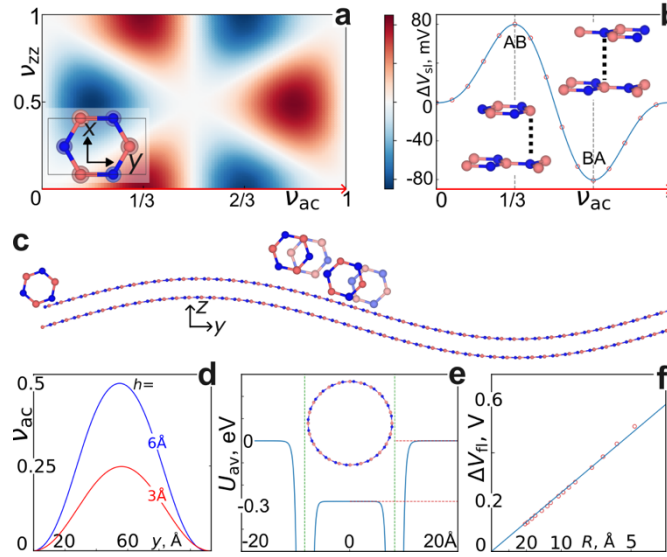


**Figure 1.** (a) A 2D map of the sliding potential step  $\Delta V_{sl}(v_{zz}, v_{ac})$ . Inset shows the used unit cell of *R*-type flat *h*BN bilayer. Different stacking configurations are created by translational sliding between two layers. (b) The sliding potential step of only armchair sliding  $\Delta V_{sl}(v_{zz} = 0, v_{ac})$ . Insets illustrate the lattices of AB and BA stacked *h*BN bilayers, reddish for boron and blue for nitrogen. (c) Side view of a *R-ac-sin* bilayer. (d) Sliding ratios throughout the *R-ac-sin* bilayer for two bending degrees:  $h = 3$  Å,  $L = 112.4$  Å and  $h = 6$  Å,  $L = 110$  Å (In both cases,  $L_0 = 113.1$  Å, which refers to the initial periodic length of flat bilayer before undulation, SI-1). (e) The average electrostatic potential  $U_{av}$  along the radial

direction of a SW-BNNT. Green dashed lines indicate the diameter of the tube. (f) The linear relationship between the flexoelectric potential step  $\Delta V_{\text{fl}}$  and tube curvature  $1/R$ .

In flat  $R$ -stacked  $h$ BN bilayer, sliding the layers along the armchair direction induces an out-of-plane polarization (Fig. 1a). We thus created an atomic structure of  $R$ -stacked  $h$ BN bilayer with sinusoidal modulation along the armchair direction (hereafter named  $R$ -*ac-sin* bilayer) (Fig. 1c). The local stacking in the undulated structure changes from  $R$ -type in the two ends to AB and BA in the middle (Fig. 1c), due to local shear changes, expected to create out-of-plane polarization (Fig. 1a,b). Undulated bilayers are distinct from the flat bilayer, as out-of-plane polarization has two contributions: from different local stacking  $\Delta V_{\text{sl}}$ , and flexoelectric polarization  $\Delta V_{\text{fl}}$  from local curvature.<sup>25-27</sup> Thus, the local total potential step across the undulated bilayer is  $\Delta V_{\text{out}}(y) = \Delta V_{\text{fl}}(y) + \Delta V_{\text{sl}}(y)$ , where "out" indicates out-of-plane direction, and  $y$  is a position in undulation direction.  $\Delta V_{\text{fl}}$  depends linearly on the local curvature  $1/R$ ,  $\Delta V_{\text{fl}} = V_0/R$ , where  $V_0$  is the flexoelectric constant, and  $R$  is radius of local circular approximation to the curve.

We obtain  $V_0 = 2.32 \text{ V}\text{\AA}$  by calculating  $\Delta V_{\text{fl}}$  for single wall boron nitride nanotubes (SW-BNNT) of different radii (Fig. 1d) using density functional theory (DFT). The red and green dots in Fig. 2a shows the out-of-plane potential step  $\Delta V_{\text{out}}(y)$ , extracted from DFT calculation, for isolated single layers (which constitutes the bilayer). In single layers,  $\Delta V_{\text{out}}(y)$  results solely from local curvature-induced flexoelectric potential, and the analytical estimate  $\Delta V_{\text{fl}}(y) = V_0/R(y)$  shown by solid green and red lines represent a good fit. In bilayers, a local stacking configuration  $C$ , depending on relative translational displacement between layers, can be mapped to an out-of-plane polarization  $C \rightarrow P$ .<sup>28</sup> Using this, we analytically estimate  $\Delta V_{\text{sl}}(y)$  by mapping local  $C(y)$  in the undulated structure to the corresponding potential step obtained from the flat configuration (Fig. 1a) with identical stacking. DFT calculations of the total potential  $\Delta V_{\text{out}}(y)_{\text{total}}$  in undulated bilayers (blue dots in Fig. 2a) align well with the blue solid line showing the analytical estimate  $\Delta V_{\text{out}}(y)_{\text{total}} = 2V_0/R(y) + \Delta V_{\text{sl}}(y)$ . To further isolate the out-of-plane polarization domains and potential change induced by "only" stacking change in an undulated bilayer, we subtract the potential from the individual layers from the total,  $\Delta V_{\text{sl}}(y) = \Delta V_{\text{out}}(y)_{\text{total}} - (\Delta V_{\text{fl}}(y)_{\text{layer,1}} + \Delta V_{\text{fl}}(y)_{\text{layer,2}})$ . (See SI-2 for more details on how to extract local potential steps.) The undulation-induced  $\Delta V_{\text{sl}}(y)$  is shown by purple color in Fig. 2a, comparing DFT calculated data (circles) with stacking-based estimates (solid curve). The alternating sign of potential steps confirm out-of-plane polarization domains in undulated bilayers, similar to the ferroelectric domains discovered recently in twisted- $h$ BN.<sup>23,24</sup> The difference being that the domains in the present case arise due to shear and are 1D. The domains' polarization can be switched by similar means as that obtained in the twisted case.

It is also non-trivial to ask the maximum magnitude of  $\Delta V_{\text{sl}}$  and  $\Delta V_{\text{fl}}$  that can be reached in a  $R$ -*ac-sin* bilayer. Since  $\Delta V_{\text{sl}}$  and  $\Delta V_{\text{fl}}$  can be estimated by local stacking  $C$  and local curvature  $1/R$ , respectively, their maximum values can be evaluated as a function of amplitude  $h$  and periodic length  $L$  (Fig. S6).  $\Delta V_{\text{sl}}$  tends to dominate unless the bending is small, and saturate when AB or BA stacking

is locally achieved. At last, it should be noted that only undulated  $R$ -stacked  $h$ BN bilayer, being not-centrosymmetric, exhibits out-of-plane polarization domains due to change in local stacking. The undulated  $H$ -stacked bilayer has local inversion symmetry, and the total out-of-plane potential step, as shown in Fig. S7, is only contributed from flexoelectric effect  $\Delta V_{\text{out}(y)}_{\text{total}} = \Delta V_{\text{fl}(y)}_{\text{layer},1} + \Delta V_{\text{fl}(y)}_{\text{layer},2}$ . Thus an undulated  $H$ -stacked bilayer does not exhibit sliding induced polarization due to  $\Delta V_{\text{sl}(y)}$  being zero.

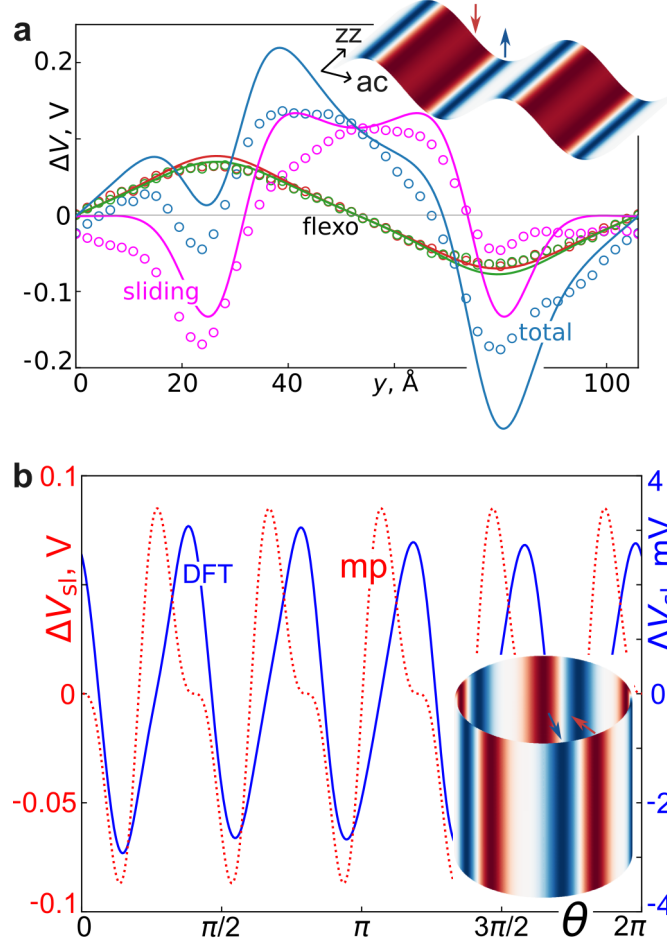


**Figure 2.** (a) Different components of the local potential step across an  $R$ - $ac$ - $sin$  bilayer with  $h = 9 \text{ \AA}$ ,  $L = 106 \text{ \AA}$ . The circles and solid curves represent data from DFT calculation and local mapping, respectively. The red and green colors refer to the local potential step purely due to bending flexoelectricity in two individual sinusoidal monolayers, of which analytical fitting is derived from the linear relationship between local curvature and flexoelectric potential step. The purple color refers to the local potential step purely due to sliding. The blue color refers to the local total potential step across the bilayer, of which analytical fitting is the addition of all components from analytical models. Inset shows an illustration of polarization domains due to sliding in the  $R$ - $ac$ - $sin$  bilayer, where arrows show out-of-plane dipole direction. (b) The sliding-induced local potential step  $\Delta V_{\text{sl}}(\theta)$  across the  $ac$ DW-BNNT. The red curve is obtained by mapping (mp) local stacking to flat configuration, while the blue curve is directly extracted from DFT at a given radius-distance  $r$ . Inset shows an illustration of polarization domains in  $ac$ DW-BNNT.

Notably, sliding induced polarization domains are also expected in double wall boron nitride nanotubes (DW-BNNT), where the different curvatures of the inner and outer tubes create shear and alter local stacking. For simplicity, we focus on armchair DW-BNNT (acDW-BNNT) with chiral indices  $(n - 5, n - 5)$  and  $(n, n)$ . In acDW-BNNT, shear occurs along the armchair direction, with local areas experiencing AB and BA stackings, which result in the maximum out-of-plane potential step. The periodicity of the shear pattern around the acDW-BNNT circumference depends on the radius difference between the tubes. For an acDW-BNNT with an intertube distance  $d = 3.46 \text{ \AA}$  and bond length  $l = 1.45 \text{ \AA}$ , the total period in shear pattern is expected to be  $2\pi d/(3l) \sim 5$ , as a shear displacement of three bond lengths completes one interlayer sliding cycle. Similar to undulated bilayers, the polarization domains in acDW-BNNT are mapped from local stacking configurations C. The red curve in Fig. 2b shows the oscillation of sliding-induced potential steps  $\Delta V_{\text{sl}}(\theta)$  due to the varying polarization domains, based on the local C  $\rightarrow$  P mapping from Fig. 1a.

To further confirm the presence of polarization domains,  $\Delta V_{\text{sl}}(r, \theta)$  from DFT calculations is plotted in the azimuthal direction  $\theta$  at a radius-distance  $r$  ( $> r_{\text{outer tube}}$ , Fig. S8), shown by the blue curve in Fig. 2b. Following the approach used for undulated bilayer *h*BN, we define  $\Delta V_{\text{sl}}(r, \theta) = \Delta V_{\text{DWNT}}(r, \theta) - \Delta V_{\text{inner}}(r, \theta) - \Delta V_{\text{outer}}(r, \theta)$ , where  $\Delta V(r, \theta) = V(r, \theta) - V_{\text{axial}}$  in respective calculation. Since the flexoelectric effect is uniform at a fixed  $r$  and does not depend on  $\theta$ ,  $\Delta V_{\text{inner}}(r, \theta)$  and  $\Delta V_{\text{outer}}(r, \theta)$ , are constants. The potential profile  $\Delta V_{\text{sl}}(r, \theta)$  has five periods, consistent with the expected shear pattern. Additionally, the agreement between the behavior of the potential profile obtained from DFT calculations and mapping from local C  $\rightarrow$  P, confirms bending-induced shear and existence of out-of-plane polarization domains in acDW-BNNT. Our examples of undulated *R*-stacked *h*BN bilayer and acDW-BNNT demonstrate the existence of sliding induced 1D out-of-plane polarization domains, resulting from shear-induced changes in local stackings.

**Undulation-induced 1D quantum-well-like states:** In addition to creating 1D ferroelectric domains, 1D undulation must also generate a moiré potential through stacking alterations, similar to twisted-moiré systems. Such a moiré potential is expected in any generic undulated 2D bilayer semiconductor, confining electrons along the undulation direction. Using sinusoidal *h*BN bilayers as an example, we illustrate the effect of undulation on the electronic structure, though it applies to any 2D semiconductor. *H*-stacked *h*BN bilayer, which lacks sliding-induced out-of-plane polarization, is considered to solely investigate the effect of moiré potential on the electronic structure. Specifically, in a *H*-stacked *h*BN bilayer sinusoidally modulated along the zigzag direction (hereafter named *H*-zz-*sin* bilayer), we investigate the electronic bands along and normal to the undulation direction, corresponding to the  $\mathbf{k}$ -path  $(\pi/L, 0, 0)$ - $(0, 0, 0)$ - $(0, \pi/L, 0)$ , noted as X- $\Gamma$ -Y. After modulation, the initially parabolic folded bands along X- $\Gamma$  (Fig. S9) at band edges (near valence band maximum, VBM, and conduction band

minimum, CBM), in flat  $H$ -stacked bilayer, become flattened and isolated, while bands along  $\Gamma$ -Y remain dispersive (Fig. 3a). As bending increases, the evolution of band edges from dispersive to flat along X- $\Gamma$  is clearly seen (Fig. S10).

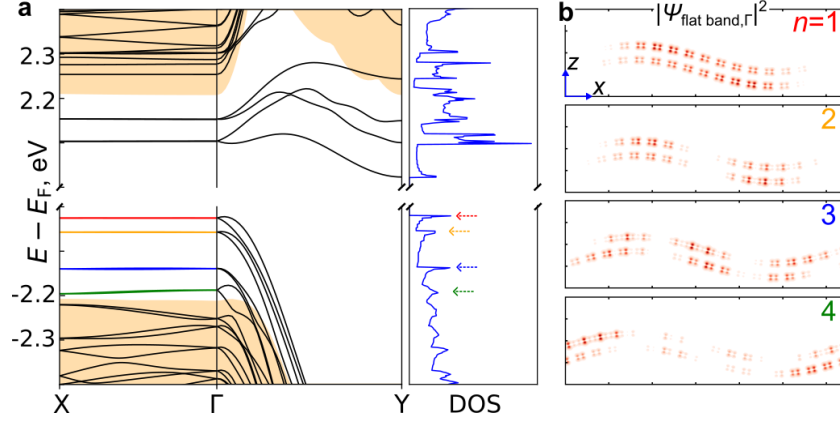


**Figure 3.** (a) Electronic band structure and density of states (DOS) from DFT calculation of  $H$ - $zz$ - $\sin$  bilayer with  $h = 3 \text{ \AA}$ ,  $L = 64 \text{ \AA}$ . Yellow-shaded areas mark the bands of flat  $H$ -stacked bilayer. The length of  $\mathbf{k}$ -path X- $\Gamma$  is rescaled for visual clarity due to the large lattice constant of modulation direction. The van Hove singularities induced by 1D states in flat valence bands are indicated by arrows. (b) The spatial distributions of electronic states,  $|\Psi_{\text{flat band},\Gamma}|^2$ , corresponding to the  $\Gamma$  point of 1D flat valence bands. All shown states are indexed by the node feature of quantum states of the 1D quantum well model individually. The color of indices follows the color of flat bands in (a) to show correspondence.

To further analyze the nature of 1D flat bands, we examine the spatial distributions of electronic states at  $\Gamma$  point,  $|\Psi_{\text{flat band},\Gamma}|^2$ . The highest 1D flat valence (double degenerated) bands (Fig. 3a red bands) are spatially-localized at one domain (Fig. 3b topmost panel,  $n = 1$  state); that of the lower 1D flat valence bands (Fig. 3a orange bands) is localized at two domains (Fig. 3b next panel,  $n = 2$  state). The states  $n = 3, 4$  are also shown. Similar localization also exists (Fig. S11) for flat conduction bands. These localized states in a series of 1D flat bands resemble the eigenfunctions of a 1D quantum well model (1D model). Generally, states with more nodes have higher energy, however, here, the 1D flat valence bands have hole characters, where the direction of increasing energy is opposite of that for electrons. The hole states with more nodes and greater dispersion appear at lower electron energy. The presence of 1D flat bands and its close resemblance with a 1D model implies the presence of a 1D electronic confinement potential throughout the undulated bilayer, arising possibly due to the moiré pattern. No such 1D flat bands or localized states are found near the VBM and CBM in an undulated monolayer (Fig. S12), indicating that the interlayer coupling in bilayer is crucial to create the modified electronic states. In an undulated bilayer, varying interlayer shear changes the local stacking and can alter the interlayer coupling, affecting the local electronic energy. Therefore, the 1D confinement moiré potential responsible for the 1D flat bands could originate from the deformation of the electronic states due to changing shear, much like the commonly studied deformation caused by tensile or compressive

strain.<sup>29</sup>

To deeply understand the origin of the moiré confinement potential, we evaluate the role of shear ( $\gamma$ ) deformation potential,  $U_\gamma(v)$ , defined as the variation in VBM across different stacking configurations in flat bilayers (Fig. S13). Note that only shear along the zigzag direction is considered. The deformation potential profile throughout an undulated bilayer,  $U_\gamma(x)$ , is determined by mapping the local stacking to the VBM of flat bilayer with identical stacking. Fig. 4a shows  $U_\gamma(x)$  for three *H-zz-sin* bilayers with varying bending. To highlight the resemblance with the 1D model,  $U_\gamma(x)$  is used as an external potential to numerically solve the 1D Schrodinger equation (1DSE)  $[-(\hbar^2/2m_c)\nabla_x^2 + U_\gamma(x)]\psi = E\psi$ . The resulting dispersions (Fig. S14) show discrete energy levels due to confinement, agreeing well with the energy eigenvalues of 1D flat valence bands obtained from DFT calculations (Fig. S15). This confirms the similarity, in terms of confinement to electrons and holes, between undulated bilayer and the 1D model, as well as that the shear deformation potential likely creates the electronic confinement.

The introduction of shear deformation potential and 1D model allows for quantifying how the band edges evolve, from dispersive to flat, when the flat bilayer gradually bends, i.e. in the limit  $h/L \rightarrow 0$ . Two quantities describing the band dispersion are of particular interest: the band width  $W$ , which is the energy range of the topmost band in the spectrum, and the energy separation  $E_s$ , which is the energy difference between the highest energy band and continuum. In the context of DFT calculation,  $W$  refers to the energy range of the highest valence band, while  $E_s$  represents the energy difference between the VBM in undulated bilayer and that in flat bilayer (Fig. S16). Both  $W$  and  $E_s$  depend on the confinement potential, determined by undulation parameters  $h$  and  $L$ . In the limit  $h/L \rightarrow 0$ , the shear deformation potential  $U_\gamma(x)$  depends quadratically on  $h/L$ , expressed as  $U_\gamma(x) = -145(1 - \cos(2\pi x/L))^2 h^2/L^2 = u_\gamma(x)h^2/L^2$  (see SI-3 for detailed derivation). This arises because  $U_\gamma$  is symmetric and independent of the bending direction, allowing a quadratic approximation for  $U_\gamma(v) = -2.19v^2$ , when the local sliding ratio  $v$  is small (Fig. S13). Additionally,  $v$  is linearly related to  $h/L$ , confirming the quadratic relationship between  $U_\gamma(x)$  and  $h/L$ .

Upon determining,  $U_\gamma(x) \propto h^2/L^2$ , the behaviors of  $W(h, L)$  and  $E_s(h, L)$  can be derived. Using the eigenvalue solutions of the Mathieu's equation,<sup>30,31</sup> (see SI-4 for more details), an analytical form of  $W(h, L) = (c_1 + c_2 h^2)/L^2$  is obtained, where  $c_{1,2}$  are fitting constants. Additionally,  $E_s(h, L)$  is determined by first-order perturbation theory,  $E_s = \langle \psi^{(0)} | U_\gamma | \psi^{(0)} \rangle = \frac{h^2}{L^2} \langle \psi^{(0)} | u_\gamma(x) | \psi^{(0)} \rangle$ , where  $\psi^{(0)}$  is the eigenstate of interest, yielding  $E_s(h, L) = c_3(h/L)^2$ , with  $c_3$  as a fitting constant. Fig. 4d shows the dependence of  $W$  (orange surface) and  $E_s$  (blue surface) on  $h$  and  $L$ . The analytical results  $W(h, L)$  and  $E_s(h, L)$  is fitted to their values obtained by numerically solving the 1DSE for various combinations of  $h$  and  $L$  (scatters in Fig. S17), showing good agreement. It can be beneficial to discuss  $W(h, L)$  behavior in three scenarios. First, as  $h$  increases with a fixed  $L$  (red line in Fig. 4d),  $W$  decreases due to stronger localization by a deeper confinement potential. Second, when  $h/L$  is fixed with increasing  $h$  or  $L$  (green line), the potential depth does not change, the decrease of  $W$  is attributed to the larger separation between

neighboring localized states. Third, with fixed  $h$  and increasing  $L$  (blue line),  $W$  tends to decrease, largely for the same reason as in the second case. The analytical equations of  $W(h, L)$  and  $E_s(h, L)$  provide a predictive framework for understanding the evolution of band edges as the bilayer bends.

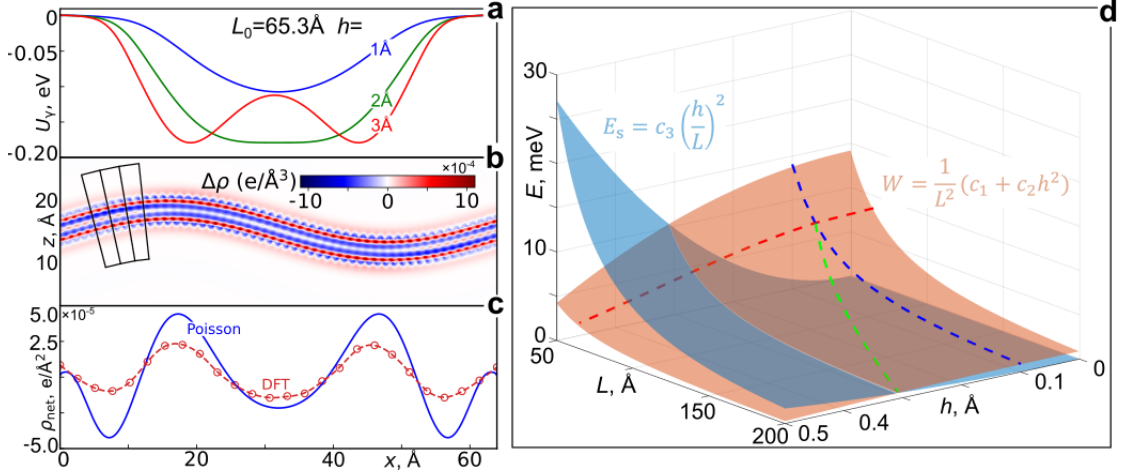


**Figure 4.** (a) Shear deformation potential profile  $U_\gamma$  as a function of position in undulation direction. Shown are the values for  $H$ - $zz$ - $\sin$  bilayer with three  $h$  values. (b) 2D map of differential charge density  $\Delta\rho$  for  $H$ - $zz$ - $\sin$  bilayer with  $h = 3 \text{ Å}$ ,  $L = 64 \text{ Å}$ . The raw data is averaged along  $y$  direction. The color scheme for plotting follows (a). (c) Comparison between  $\rho_{\text{net}}$  extracted from DFT-calculated  $\Delta\rho$  (red) and charge density distribution analytically solved from  $U_\gamma(x)$  by Poisson's equation (blue). (d) The dependence of band width  $W$  (orange surface) and energy separation from continuum  $E_s$  (blue surface) on  $h$  and  $L$ , plotted according to the analytical equations.

It should be noted that the  $H$ - $zz$ - $\sin$  bilayer shows no out-of-plane polarization, and the electronic confinement arises solely from a modulating shear deformation potential along the tangential direction, due to varying interlayer shear in the 1D moiré pattern. This modulating confinement potential must be driven by charge redistribution, in turn creating a tangential polarization. To verify charge redistribution along the tangential direction in the undulated bilayer, we examined local charge density changes  $\Delta\rho(x)$ , which reveal electrostatically non-neutral regions in  $H$ - $zz$ - $\sin$  bilayer. Using differential charge density  $\Delta\rho = \rho_{\text{bilayer}} - \rho_{\text{single\_layer1}} - \rho_{\text{single\_layer2}}$ , and a macroscopic averaging technique, which is tailored for layered atomic structure with curvature (see [Method](#) for more details), the local net charge density  $(\Delta\rho)_{\text{ave}}$  was calculated, shown in [Fig. 4b](#).  $(\Delta\rho)_{\text{ave}} = \int_V \Delta\rho dV/V$ , where  $V$  represents a local volume for macroscopic averaging, depicted by the black box. The selection of  $V$  ensures that its in-plane (parallel to atomic structure) dimensions match the  $xy$  plane of the rectangular unit cell ([Fig. 1a](#) inset), and its out-of-plane (normal to atomic structure) dimension is sufficiently large to ensure convergence in the average charge density calculation. If  $(\Delta\rho)_{\text{ave}}$  is zero, neutral condition is retained in the local region, which is always true in flat bilayer configuration; otherwise, charge flow occurs along the tangential direction. To give a more intuitive physical quantity, we define the local net charge density per area as  $\rho_{\text{net}} = (\Delta\rho)_{\text{ave}}/ab$ , where  $a$  and  $b$  are lattice constants of the rectangular unit cell ([Fig.](#)

1a) for zigzag and armchair direction, respectively. Red curve in Fig. 4c shows  $\rho_{\text{net}}$  of different regions throughout the undulated bilayer, where 26 unique values are obtained, corresponding to 26 rectangular unit cells in building the supercell of sinusoidal structure (SI-1). A negative and positive net charge density indicates a negatively and positively charged local area, respectively. Therefore, the charge redistribution along the tangential direction is verified directly from the results of DFT calculation. The  $\rho_{\text{net}}$  is also compared with the charge density distribution corresponding to the shear deformation potential  $U_{\gamma}(x)$ , solved from Poisson's equation  $\nabla^2 U_{\gamma}(x) = \rho_{\text{net}}(x)/\epsilon_0$  (blue curve in Fig. 4c), and the trends are in agreement. Accordingly, the shear-induced deformation potential through the undulated bilayer is proved to be the main cause of the 1D flat bands. To better convey the idea, a simple tight-binding model is constructed to illustrate that 1D confining potential can unidirectionally flatten electronic bands in flat *h*BN monolayer (SI-5). In undulated bilayers, shear deformation potential serves as such a confinement.

We emphasize that charge redistribution in the tangential direction, which creates the shear deformation potential, leads to the presence of in-plane dipole moments. In *H*-stacked *h*BN bilayer with inversion symmetry, no polarization in the flat configuration, unlike the intrinsic in-plane 2D ferroelectrics,<sup>32</sup> this tangential polarization from the 1D moiré pattern drives the electronic confinement and 1D flat bands. However, this in-plane polarization has been rarely discussed in the recent slidetronics works of 2D moiré systems, and the condition of *H*-stacked bilayer is completely overlooked. It could be insightful to investigate the detailed polarization texture in the moiré-based configurations.

The 1D quantum-well-like flat bands along X- $\Gamma$  are also present in *R*-stacked *h*BN bilayer sinusoidally modulated in the zigzag direction (*R*-*zz-sin* bilayer). Although the distribution of  $|\Psi_{\text{flat}}|_{\text{band},\Gamma}^2$  is less regular, but the quantum-well-like node character is still observable (Fig. S18), indicating that the origin of these 1D bands does not depend on the specific stacking. It is worth mentioning that sinusoidal modulation along armchair direction in either *H*- or *R*-stacked *h*BN bilayer (*H-ac-sin* and *R-ac-sin* bilayer) can also create similar 1D flat bands along  $\Gamma$ -Y, rather than X- $\Gamma$  (Fig. S19). However, the electronic bands along  $\Gamma$ -Y in such systems reside at deep energy levels, which are far below (above) the VBM (CBM), thus rendering them not of much interest. Hence, only *h*BN bilayers undulated along the zigzag direction can create 1D quantum-well-like states near the valence and conduction band. These 1D states display van Hove singularities, which if accessed upon electron/hole doping, can be a novel physical system to realize strongly correlated physics phenomena, such as superconductivity, magnetism, strongly correlated electronic phases, etc.<sup>33-35</sup> Additionally, the 1D feature may offer a way to mimic the multiband materials with quasi-1D band in the context of superconductivity<sup>16,36-38</sup> and electronic anisotropy,<sup>11,39</sup> and study the interplay between quasi-1D states and states with high dimensional characteristics.<sup>40</sup> On the other hand, these 1D bands are analogous to those in widely studied 1D quantum wells based on bulk III-V semiconductors.<sup>41</sup> Similar to 1D quantum wells, these 1D states in undulated 2D bilayers can greatly enhance the lifetime of photogenerated carriers and

increase the overall performance of devices based on such effects, which are beneficial for applications in quantum cascade lasers, enhanced photogenerated carrier efficiency for photovoltaics, LEDs, and photodiodes (see SI-6 for more discussions on possible applications<sup>42,43</sup>).

## Conclusions

In conclusion, we have shown that a 1D undulation of a 2D van der Waals bilayer can generate a 1D moiré pattern, inducing sliding-induced ferroelectric domains paired with flexoelectric polarization. The idea is also extended to DW-BNNT, where the texture of polarization domains in acDW-BNNT is discussed. The sliding-induced polarization domains are similar to those in recently discovered twisted-moiré systems and can be switched to demonstrate 1D ferroelectric behavior. Additionally, the out-of-plane polarization due to undulations is an outcome of a combined effect of sliding-induced ferroelectricity and curvature-induced flexoelectricity, which increases the magnitude of surface potential modulation on either side (top/bottom) of the layers. We find that a total modulation of  $\Delta V_{\text{out}} \sim 0.5$  eV (Fig. 2a) can be achieved in such undulated layers with moderate aspect ratios  $h/L < 0.1$ . This large  $V_{\text{out}}$  can alter the band positions of another functional layer like MoS<sub>2</sub>, when stacked on top of the undulated *h*BN bilayer and can significantly impede exciton diffusion<sup>44</sup> and modulate the optical properties of the functional layer.

On the other hand, by choosing a specific modulation direction, the emergence of 1D flat bands due to 1D moiré confinement potential in undulated *h*BN bilayer is achieved at the top/bottom of valence/conduction bands. The confinement potential is attributed to shear deformation potential modulation arising from the tangential polarization due to the moiré pattern. Such in-plane polarization has been overlooked before in moiré-based systems until a recent study exclusively focused on *R*-stacked *h*BN bilayer,<sup>28</sup> and must be included to get accurate representation of the polarization textures. The 1D confinement potential in undulated *h*BN bilayer itself is also expected to confine excitons and realize highly anisotropic exciton flow.<sup>45</sup> The 1D quantum-well-like flat bands display van Hove singularities, which if accessed upon proper electron/hole doping can be employed to study strongly correlated physics in 1D. Moreover, due to the similarity between localized states in 1D flat bands and those in conventional quantum wells, these states can be exploited to design related high-performance functional devices, such as quantum cascade laser, photovoltaics, LEDs and more.<sup>42,43</sup>

## Methods

**First-principles calculations:** Density functional theory (DFT) calculations were performed using DFT-D2 vdW approach<sup>46</sup> in conjunction with the Perdew–Burke–Ernzerhof (PBE) generalized gradient approximation<sup>47</sup> in the framework of the all-electron projector augmented wave (PAW) method<sup>48</sup> as implemented in the Vienna Ab-initio Simulation Package.<sup>49</sup> The plane-wave kinetic energy cutoff was 500 eV. To eliminate the interactions between the double layer with its periodic images, the

length of the supercell constant in  $z$  direction has been set as  $30\text{\AA}$ . For  $R$ - or  $H$ - $zz$  ( $R$ - or  $H$ - $ac$ ) bilayer,  $k$ -mesh of  $1\times 20\times 1$  ( $20\times 1\times 1$ ) was used in self-consistent field calculation until the total energy was converged to  $10^{-5}\text{eV}$ . To keep the interlayer shear pattern by design, structure optimization was conducted separately for two individual sinusoidal monolayers. The atomic positions almost do not change during structure relaxation, which can be expected since no intralayer strain is introduced when assigning sinusoidal modulation. Simply stacking two monolayers together generates the bilayer used in the following electronic band calculation. The  $\mathbf{k}$ -path  $(\pi/L, 0, 0)$ - $(0, 0, 0)$ - $(0, \pi/L, 0)$ , noted as X- $\Gamma$ -Y, in the Brillouin zone is used, which has absolutely different values for supercells with different sizes.

**Macroscopic averaging:** Macroscopic averaging is performed upon a 2D grid data set of charge density (encoded in  $x$  and  $z$  coordinates, for a  $H$ - $zz$ - $sin$  bilayer), which is derived by averaging the raw volumetric data along  $y$  direction (the direction without undulation in a  $H$ - $zz$ - $sin$  bilayer). The idea is to partition the central line between two layers (two curves in the projected  $xz$  plane) into 26 pieces, corresponding to the 26 rectangular unit cells in building the supercell of sinusoidal structure. The length of each segment equals the lattice constant of zigzag direction in the unit cell. The tangential size of averaging window, black box in Fig. 4b, follows these segments and the two longer sides are strictly normal to the central line and the two layers. Therefore, the averaging window has a shape of rectangle when the local curvature of the atomic structure is zero, such as left/right end and mid, otherwise, a shape of trapezoid, while the size of the averaging window is fixed. In each averaging window, average charge density difference can be calculated by  $(\Delta\rho)_{\text{ave}} = \int_V \Delta\rho dV$ .

## References

- (1) Novoselov, K. S.; Mishchenko, A.; Carvalho, A.; Castro Neto, A. H. 2D Materials and van Der Waals Heterostructures. *Science* **2016**, *353* (6298), aac9439.
- (2) Carr, S.; Massatt, D.; Fang, S.; Cazeaux, P.; Luskin, M.; Kaxiras, E. Twistronics: Manipulating the Electronic Properties of Two-Dimensional Layered Structures through Their Twist Angle. *Phys. Rev. B* **2017**, *95* (7), 075420.
- (3) Bistritzer, R.; MacDonald, A. H. Moiré Bands in Twisted Double-Layer Graphene. *Proc. Natl. Acad. Sci.* **2011**, *108* (30), 12233.
- (4) Kennes, D. M.; Claassen, M.; Xian, L.; Georges, A.; Millis, A. J.; Hone, J.; Dean, C. R.; Basov, D. N.; Pasupathy, A. N.; Rubio, A. Moiré Heterostructures as a Condensed-Matter Quantum Simulator. *Nat. Phys.* **2021**, *17* (2), 155.
- (5) Fox, C.; Mao, Y.; Zhang, X.; Wang, Y.; Xiao, J. Stacking Order Engineering of Two-Dimensional Materials and Device Applications. *Chem. Rev.* **2024**, *124* (4), 1862.
- (6) Wu, M.; Li, J. Sliding Ferroelectricity in 2D van Der Waals Materials: Related Physics and Future Opportunities. *Proc. Natl. Acad. Sci.* **2021**, *118* (50), e2115703118.
- (7) Gupta, S.; Li, X.; Yakobson, B. I. Shear-Induced Electronic Confinement and One-Dimensional Bands

- in Two-Dimensional Undulated Bilayer Semiconductors. In *Bulletin of the American Physical Society* **2024**.
- (8) Levy, N.; Burke, S. A.; Meaker, K. L.; Panlasigui, M.; Zettl, A.; Guinea, F.; Neto, A. H. C.; Crommie, M. F. Strain-Induced Pseudo-Magnetic Fields Greater Than 300 Tesla in Graphene Nanobubbles. *Science* **2010**, *329* (5991), 544.
  - (9) Guinea, F.; Katsnelson, M. I.; Geim, A. K. Energy Gaps and a Zero-Field Quantum Hall Effect in Graphene by Strain Engineering. *Nat. Phys.* **2010**, *6* (1), 30.
  - (10) Mao, J.; Milovanović, S. P.; Anđelković, M.; Lai, X.; Cao, Y.; Watanabe, K.; Taniguchi, T.; Covaci, L.; Peeters, F. M.; Geim, A. K.; Jiang, Y.; Andrei, E. Y. Evidence of Flat Bands and Correlated States in Buckled Graphene Superlattices. *Nature* **2020**, *584* (7820), 215.
  - (11) Ho, S.-C.; Chang, C.-H.; Hsieh, Y.-C.; Lo, S.-T.; Huang, B.; Vu, T.-H.-Y.; Ortix, C.; Chen, T.-M. Hall Effects in Artificially Corrugated Bilayer Graphene without Breaking Time-Reversal Symmetry. *Nat. Electron.* **2021**, *4* (2), 116.
  - (12) Yu, H.; Kutana, A.; Yakobson, B. I. Electron Optics and Valley Hall Effect of Undulated Graphene. *Nano Lett.* **2022**, *22* (7), 2934.
  - (13) Milovanović, S. P.; Anđelković, M.; Covaci, L.; Peeters, F. M. Band Flattening in Buckled Monolayer Graphene. *Phys. Rev. B* **2020**, *102* (24), 245427.
  - (14) Gupta, S.; Yu, H.; Yakobson, B. I. Designing 1D Correlated-Electron States by Non-Euclidean Topography of 2D Monolayers. *Nat. Commun.* **2022**, *13* (1), 3103.
  - (15) Liu, Y.; Rodrigues, J. N. B.; Luo, Y. Z.; Li, L.; Carvalho, A.; Yang, M.; Laksono, E.; Lu, J.; Bao, Y.; Xu, H.; Tan, S. J. R.; Qiu, Z.; Sow, C. H.; Feng, Y. P.; Neto, A. H. C.; Adam, S.; Lu, J.; Loh, K. P. Tailoring Sample-Wide Pseudo-Magnetic Fields on a Graphene-Black Phosphorus Heterostructure. *Nat. Nanotechnol.* **2018**, *13* (9), 828.
  - (16) Tang, E.; Fu, L. Strain-Induced Partially Flat Band, Helical Snake States and Interface Superconductivity in Topological Crystalline Insulators. *Nat. Phys.* **2014**, *10* (12), 964.
  - (17) Mucha-Kruczyński, M.; Aleiner, I. L.; Fal'ko, V. I. Strained Bilayer Graphene: Band Structure Topology and Landau Level Spectrum. *Phys. Rev. B* **2011**, *84* (4), 041404.
  - (18) Pereira, V. M.; Castro Neto, A. H. Strain Engineering of Graphene's Electronic Structure. *Phys. Rev. Lett.* **2009**, *103* (4), 046801.
  - (19) Bolotin, K. I.; Sikes, K. J.; Jiang, Z.; Klima, M.; Fudenberg, G.; Hone, J.; Kim, P.; Stormer, H. L. Ultrahigh Electron Mobility in Suspended Graphene. *Solid State Commun.* **2008**, *146* (9), 351.
  - (20) Rhee, D.; Paci, J. T.; Deng, S.; Lee, W.-K.; Schatz, G. C.; Odom, T. W. Soft Skin Layers Enable Area-Specific, Multiscale Graphene Wrinkles with Switchable Orientations. *ACS Nano* **2020**, *14* (1), 166.
  - (21) Banerjee, R.; Nguyen, V.-H.; Granzier-Nakajima, T.; Pabbi, L.; Lherbier, A.; Binion, A. R.; Charlier, J.-C.; Terrones, M.; Hudson, E. W. Strain Modulated Superlattices in Graphene. *Nano Lett.* **2020**, *20* (5), 3113.
  - (22) Blees, M. K.; Barnard, A. W.; Rose, P. A.; Roberts, S. P.; McGill, K. L.; Huang, P. Y.; Ruyack, A. R.; Kevek, J. W.; Kobrin, B.; Muller, D. A.; McEuen, P. L. Graphene Kirigami. *Nature* **2015**, *524* (7564),

204.

- (23) Vizner Stern, M.; Waschitz, Y.; Cao, W.; Nevo, I.; Watanabe, K.; Taniguchi, T.; Sela, E.; Urbakh, M.; Hod, O.; Ben Shalom, M. Interfacial Ferroelectricity by van Der Waals Sliding. *Science* **2021**, 372 (6549), 1462.
- (24) Yasuda, K.; Wang, X.; Watanabe, K.; Taniguchi, T.; Jarillo-Herrero, P. Stacking-Engineered Ferroelectricity in Bilayer Boron Nitride. *Science* **2021**, 372 (6549), 1458.
- (25) Dumitrică, T.; Landis, C. M.; Yakobson, B. I. Curvature-Induced Polarization in Carbon Nanoshells. *Chem. Phys. Lett.* **2002**, 360 (1), 182.
- (26) Kvashnin, A. G.; Sorokin, P. B.; Yakobson, B. I. Flexoelectricity in Carbon Nanostructures: Nanotubes, Fullerenes, and Nanocones. *J. Phys. Chem. Lett.* **2015**, 6 (14), 2740.
- (27) Artyukhov, V. I.; Gupta, S.; Kutana, A.; Yakobson, B. I. Flexoelectricity and Charge Separation in Carbon Nanotubes. *Nano Lett.* **2020**, 20 (5), 3240.
- (28) Bennett, D.; Chaudhary, G.; Slager, R.-J.; Bousquet, E.; Ghosez, P. Polar Meron-Antimeron Networks in Strained and Twisted Bilayers. *Nat. Commun.* **2023**, 14 (1), 1629.
- (29) Bardeen, J.; Shockley, W. Deformation Potentials and Mobilities in Non-Polar Crystals. *Phys. Rev.* **1950**, 80 (1), 72.
- (30) Arzamasovs, M.; Liu, B. Tight-Binding Tunneling Amplitude of an Optical Lattice. *Eur. J. Phys.* **2017**, 38 (6), 065405.
- (31) Olver, F. W. J.; Olde Daalhuis, A. B.; Lozier, D. W.; Schneider, B. I.; Boisvert, R. F.; Clark, C. W.; Miller, B. R.; Saunders, B. V.; Cohl, H. S.; McClain, M. A. [DLMF] *NIST Digital Library of Mathematical Functions*. <https://dlmf.nist.gov/>, Release 1.2.2 of 2024-09-15.
- (32) Barraza-Lopez, S.; Fregoso, B. M.; Villanova, J. W.; Parkin, S. S. P.; Chang, K. Colloquium: Physical Properties of Group-IV Monochalcogenide Monolayers. *Rev. Mod. Phys.* **2021**, 93 (1), 011001.
- (33) González, J.; Guinea, F.; Vozmediano, M. A. H. Kinematics of Electrons near a Van Hove Singularity. *Phys. Rev. Lett.* **2000**, 84 (21), 4930.
- (34) Fleck, M.; Oleś, A. M.; Hedin, L. Magnetic Phases near the Van Hove Singularity in  $s$ - and  $d$ -Band Hubbard Models. *Phys. Rev. B* **1997**, 56 (6), 3159.
- (35) Li, G.; Luican, A.; Lopes dos Santos, J. M. B.; Castro Neto, A. H.; Reina, A.; Kong, J.; Andrei, E. Y. Observation of Van Hove Singularities in Twisted Graphene Layers. *Nat. Phys.* **2010**, 6 (2), 109.
- (36) Bianconi, A.; Valletta, A.; Perali, A.; Saini, N. L. High  $T_c$  Superconductivity in a Superlattice of Quantum Stripes. *Solid State Commun.* **1997**, 102 (5), 369.
- (37) Jiang, H.; Cao, G.; Cao, C. Electronic Structure of Quasi-One-Dimensional Superconductor  $K_2Cr_3As_3$  from First-Principles Calculations. *Sci. Rep.* **2015**, 5 (1), 16054.
- (38) Tang, Z.-T.; Bao, J.-K.; Liu, Y.; Sun, Y.-L.; Ablimit, A.; Zhai, H.-F.; Jiang, H.; Feng, C.-M.; Xu, Z.-A.; Cao, G.-H. Unconventional Superconductivity in Quasi-One-Dimensional  $Rb_2Cr_3As_3$ . *Phys. Rev. B* **2015**, 91 (2), 020506.
- (39) Wang, X. F.; Roncaioli, C.; Eckberg, C.; Kim, H.; Yong, J.; Nakajima, Y.; Saha, S. R.; Zavalij, P. Y.; Paglione, J. Tunable Electronic Anisotropy in Single-Crystal  $A_2Cr_3As_3$  ( $A = K, Rb$ ) Quasi-One-

- Dimensional Superconductors. *Phys. Rev. B* **2015**, *92* (2), 020508.
- (40) Saraiva, T. T.; Cavalcanti, P. J. F.; Vagov, A.; Vasenko, A. S.; Perali, A.; Dell'Anna, L.; Shanenko, A. A. Multiband Material with a Quasi-1D Band as a Robust High-Temperature Superconductor. *Phys. Rev. Lett.* **2020**, *125* (21), 217003.
- (41) Schneider, H.; Klitzing, K. v. Thermionic Emission and Gaussian Transport of Holes in a GaAs/Al<sub>x</sub>Ga<sub>1-x</sub>As Multiple-Quantum-Well Structure. *Phys. Rev. B* **1988**, *38* (9), 6160.
- (42) Sayed, I.; Bedair, S. M. Quantum Well Solar Cells: Principles, Recent Progress, and Potential. *IEEE J. Photovolt.* **2019**, *9* (2), 402.
- (43) Fox, A. M.; Miller, D. A. B.; Livescu, G.; Cunningham, J. E.; Jan, W. Y. Quantum Well Carrier Sweep out: Relation to Electroabsorption and Exciton Saturation. *IEEE J. Quantum Electron.* **1991**, *27* (10), 2281.
- (44) Kim, D. S.; Dominguez, R. C.; Mayorga-Luna, R.; Ye, D.; Embley, J.; Tan, T.; Ni, Y.; Liu, Z.; Ford, M.; Gao, F. Y.; Arash, S.; Watanabe, K.; Taniguchi, T.; Kim, S.; Shih, C.-K.; Lai, K.; Yao, W.; Yang, L.; Li, X.; Miyahara, Y. Electrostatic Moiré Potential from Twisted Hexagonal Boron Nitride Layers. *Nat. Mater.* **2024**, *23* (1), 65.
- (45) Dirnberger, F.; Ziegler, J. D.; Faria Junior, P. E.; Bushati, R.; Taniguchi, T.; Watanabe, K.; Fabian, J.; Bougeard, D.; Chernikov, A.; Menon, V. M. Quasi-1D Exciton Channels in Strain-Engineered 2D Materials. *Sci. Adv.* **2021**, *7* (44), eabj3066.
- (46) Grimme, S. Semiempirical GGA-type density functional constructed with a long-range dispersion correction. *J. Comput. Chem.* **2006**, *27* (15), 1787.
- (47) Perdew, J. P.; Burke, K.; Ernzerhof, M. Generalized Gradient Approximation Made Simple. *Phys. Rev. Lett.* **1996**, *77* (18), 3865.
- (48) Blöchl, P. E. Projector Augmented-Wave Method. *Phys. Rev. B* **1994**, *50* (24), 17953.
- (49) Kresse, G.; Furthmüller, J. Efficient Iterative Schemes for Ab Initio Total-Energy Calculations Using a Plane-Wave Basis Set. *Phys. Rev. B* **1996**, *54* (16), 11169.